

DISK EVOLUTION IN THE ORION OB1 ASSOCIATION

NURIA CALVET,¹ CESAR BRICEÑO,² JESUS HERNÁNDEZ,² SERGIO HOYER,³ LEE HARTMANN,¹
AURORA SICILIA-AGUILAR,¹ S. T. MEGEATH,¹ AND PAOLA D’ALESSIO⁴

Received 2004 July 6; accepted 2004 October 13

ABSTRACT

We analyze multiband photometry of a subsample of low-mass stars in the associations Ori OB1a and 1b discovered during the Centro de Investigaciones de Astronomía (CIDA) Orion Variability Survey, which have ages of 7–10 and 3–5 Myr, respectively. We obtained $UBVR_C I_C$ photometry at Mount Hopkins for six classical T Tauri stars (CTTSs) and 26 weak T Tauri stars (WTTSs) in Ori OB1a and for 21 CTTSs and two WTTSs in Ori OB1b. We also obtained L -band photometry for 14 CTTSs at Mount Hopkins and 10 and 18 μm photometry with OSCIR at Gemini for six CTTSs; of these, all six were detected at 10 μm , whereas only one was detected at 18 μm . We estimate mass accretion rates from the excess luminosity at U and find that they are consistent with determinations for a number of other associations, with or without high-mass star formation. The observed decrease of mass accretion rate with age is qualitatively consistent with predictions of viscous evolution of accretion disks, although other factors can also play a role in slowing accretion rates. We compare the excesses over photospheric fluxes in $H - K$, $K - L$, and $K - N$ with the younger sample of Taurus and find an overall decrease of disk emission from Taurus to Ori OB1b to Ori OB1a. This decrease implies that significant grain growth and settling toward the midplane has taken place in the inner disks of Ori OB1. We compare the spectral energy distribution of the star detected at both 10 and 18 μm with disk models for similar stellar and accretion parameters. We find that the low fluxes shortward of 18 μm of this Ori OB1b star cannot be due to the smaller disk radius expected from viscous evolution in the presence of the far-ultraviolet radiation fields from the OB stars in the association. Instead, we find that the disk of this star is essentially a flat disk, with little if any flaring, indicating a significant degree of dust settling toward the midplane, as expected from dust evolution in protoplanetary disks.

Key words: accretion, accretion disks — infrared: stars — stars: formation — stars: pre-main-sequence — techniques: photometric

1. INTRODUCTION

Most star formation studies are based on a few nearby associations without massive stars, like Taurus and Chameleon, or highly populated clusters with significant high-mass star formation, like the Orion Nebula Cluster (ONC). In recent years, several teams have begun systematic studies of the populations of the OB associations. These associations cover large volumes in the sky and include populations covering the entire stellar mass range. OB associations have been the subjects of studies with *Hipparcos* (Brown et al. 1994; de Zeeuw et al. 1999), which has helped pinpoint their distances and mean ages. In a number of associations, the populations display a gradient of ages, from ~ 1 to a few tens of megayears, which has been interpreted as the result of triggered star formation (Blaauw 1964). This range of ages makes the OB associations the most suitable laboratory for studies of protoplanetary disk evolution, because it encompasses the time span in which giant planets are expected to form (Pollack et al. 1996; Alibert et al. 2004) and significant solid evolution is expected to take place, as indicated by meteoritic evidence (Podosek & Cassen 1996; Wood 2004).

We are carrying out a photometric and spectroscopic survey of $\sim 128^\circ$ in the Orion OB1 association in order to identify the low-mass population. Initial results of this survey have been presented by Briceño et al. (2001, 2005, hereafter Paper I). In Paper I, we identified 197 new low-mass members in the sub-associations Ori OB1a and 1b, spanning the mass range from ~ 0.2 to $1.4 M_\odot$. We found ages of ~ 3 –5 Myr for Ori OB1b and ~ 7 –10 Myr for Ori OB1a, confirming age determinations based on the OB stars (Blaauw 1964; Warren & Hesser 1977, 1978; Brown et al. 1994). We also found that Ori OB1b could be identified with a population associated with a ring of low-density gas and dust, probably formed by a supernova event, with most of the classical T Tauri stars (i.e., stars accreting from circumstellar disks; CTTSs) near the ring, similar to the case of λ Ori (Dolan & Mathieu 1999, 2001, 2002). In contrast, Ori OB1a is in a region devoid of gas and dust, in agreement with its older age. We also found that the number of CTTSs decreases sharply between Ori OB1b and 1a, indicating that few disks remain by ~ 10 Myr, in agreement with findings from young clusters, some containing high-mass stars, and low-mass associations like TW Hya (Haisch et al. 2001; Hillenbrand et al. 2005; Sicilia-Aguilar et al. 2005; Muzerolle et al. 2000, 2001).

In this work, we present multiwavelength photometry of a subset of the stars in Paper I, including stars in Ori OB1a, 1b, and 1c. In particular, we have obtained U photometry of a significant number of CTTSs in these subassociations, from which we have determined mass accretion rates for comparison with disk evolution theories. We have also obtained L -band and mid-infrared (IR) measurements at 10 and 18 μm of a small subset of stars in Ori OB1, which has allowed us to make assessments of

¹ Smithsonian Astrophysical Observatory, Mail Stop 42, Cambridge, MA 02138; ncalvet@cfa.harvard.edu, hartmann@cfa.harvard.edu.

² Centro de Investigaciones de Astronomía, Apdo. Postal 264, Mérida 5101-A, Venezuela; bricenoc@cida.ve, jesush@cida.ve, avivas@cida.ve.

³ Departamento Astronomía y Astrofísica, Pontificia Universidad Católica de Chile, Campus San Joaquín, Vicuña Mackenna 4860 Casilla 306 Santiago 22, Chile.

⁴ Centro de Radioastronomía y Astrofísica, Apdo. Postal 72-3 (Xangari), 58089 Morelia, Michoacán, Mexico.

the state of the dust in their disks in comparison with younger populations. In § 2 we present the photometry, and in § 3 we examine the properties of the disks in Ori OB1a and 1b in comparison with the Taurus populations. We discuss the implications of these results for disk evolution in § 4.

2. OBSERVATIONS AND DATA ANALYSIS

The targets were selected from the sample of the Orion variability survey presented in Paper I, which were originally found on the basis of variability in the V band using the QUEST camera on the 1 m Schmidt Telescope on the Venezuela National Observatory. Follow-up spectroscopy, using the FAST Spectrograph (Fabricant et al. 1998) on the 1.5 m telescope of the Fred Lawrence Whipple Observatory (FLWO) at Mount Hopkins and the Hydra multifiber spectrograph (Barden & Armandroff 1995) on the WYIN 3.5 m telescope at Kitt Peak, confirmed their membership to Ori OB1 (cf. Paper I).

2.1. Optical Photometry

We used the 4SHOOTER CCD array on the 1.2 m telescope of the FLWO on Mount Hopkins during two observing runs to obtain $UBVR_C I_C$ photometry of our list of stars. The first run was during the nights of 2002 November 29 through December 4, although observations could be done only in the second half of the night of December 3 and all night on December 4. The second run was during 2003 October 15–20. All six nights were clear. The seeing was between $1''.2$ and $2''.5$ throughout the observations. The 4SHOOTER camera contains four 2048×2048 Loral CCDs separated by $45''$ and arranged in a 2×2 grid. After binning 2×2 during readout, the plate scale was $0''.67$ pixel $^{-1}$. In order to achieve more uniform and consistent measurements, we placed all the target standard stars on the same CCD detector (chip 3).

We obtained $BVR_C I_C$ photometry for 65 stars in Ori OB1a, 1b, and 1c, and U -band photometry for 59 of these stars. In particular, out of 36 stars in Ori OB1a, we obtained U photometry for all six CTTs and 26 WTTs; for the 27 stars in Ori OB1b, we obtained U photometry for the two WTTs and 21 CTTs; finally, we obtained U photometry for the two CTTs observed in Ori OB1c.

The basic processing of the FLWO data was done with IRAF⁵ routines in the standard way. For both runs, the U -band data were flat-fielded using sky flats taken at dusk/dawn. Instrumental magnitudes were obtained using the APPHOT package in IRAF. Although Orion is at a moderately low Galactic latitude, $b \sim -20^\circ$, our fields are not crowded in the relevant magnitude range, so aperture photometry is adequate. We used an aperture radius of 15 pixels for the source, ~ 4 times the typical 3.5 pixel FWHM of our observations, large enough to include all the light from the standard stars, as well as some observations made under mediocre seeing. We used a sky annulus of 15 and 20 pixels for the inner and outer radii, respectively. The instrumental magnitudes were calibrated in the Johnson UBV and Cousins RI system with observations of Landolt (1992) standard fields SA 92, SA 95, SA 113, and PG 0231+051 at various air masses every night; each field contains stars with a range of colors similar to our target objects. Our overall photometric errors are dominated by the transformation uncertainty, which is 0.05 mag in U and 0.02 mag for $BV(RI)_C$. The nightly variation in the zero points was 0.15, 0.07, 0.06, 0.04, and 0.05 mag $UBV(RI)_C$,

respectively, suggesting reasonably good photometric stability throughout both runs.

The resulting photometry is listed in Table 1, where stars are identified by their running numbers in Paper I. Two exposures in some bands were obtained for star CVSO 35 in Ori OB1a and for stars CVSO 146 and 190 in Ori OB1b, as indicated in Table 1.

2.2. Near-Infrared Photometry

We obtained L -band photometry for a subsample of 14 stars using the dual-channel IR camera STELIRCam (Tollestrup & Willner 1998) on the 1.2 m telescope at FLWO during the nights of 2002 December 18–19. STELIRCam consists of two 256×256 pixel InSb detector arrays. Each is fed from a dichroic mirror that separates wavelengths longer and shorter than $1.9 \mu\text{m}$ into two independent imaging channels (red and blue channels) for simultaneous observations on the sky. Three separate magnifications can be selected by rotating cold lens assemblies into the beam. The magnification is the same in both wavelength channels. For our observations we used the medium lens, yielding a scale of 0.6 pixel $^{-1}$ and a $2'.5 \times 2'.5$ field of view, together with the L -Barr filter ($3.5 \mu\text{m}$) in the red channel. To convert the instrumental magnitudes of STELIRCam to the standard system, stars BD $+0^\circ 1694$, G77-31, Gl 105.5, Gl 406, HD 1160, HD 18881, HD 225023, and HD 40335 from the list of Elias et al. (1982) were observed each night at various air masses. Both the Orion and standard stars were observed with a 3×3 square pattern with $20''$ dither between positions. The integration time at each dither position was 10 s (0.1×100 co-additions).

All data were first linearized using frames obtained at various exposure times and routines developed in the Interactive Data Language (IDL) by T. Megeath at the Center for Astrophysics. We then used standard IRAF routines to proceed with the data reduction. Average dark frames were constructed from darks taken at the beginning and end of each night's observations. These average dark frames were then subtracted from each image. Sky frames were individually made for each observation by median-combining the nine unregistered frames in one dither pattern. The sky frames were subtracted from each image within the dither set. The high- and low-airmass frames were grouped into pairs, and the low-airmass frame in each pair was subtracted from the high-airmass frame. These subtracted pairs were then normalized and the pairs combined using a median statistic to create the flat field.

Typically only the target star was visible in the L -band images, with a FWHM ranging from ~ 2.3 to 3 pixels. Thus, we measured instrumental magnitudes with the IRAF APPHOT package, using an aperture radius of 6 pixels and a sky annulus with inner and outer radii of 10 and 20 pixels, respectively, for both Orion and standard stars. After obtaining the zero points and color terms (which were small), we arrived at an L -band 1σ error of 0.07 mag, mostly dominated by measurement errors.

The L -band photometry is presented in Table 1, where we also include Two Micron All Sky Survey (2MASS) JHK_s magnitudes for the stars from Paper I.

2.3. Mid-Infrared Photometry

We obtained mid-IR photometry of a subsample of six stars in Ori OB1a and B, using OSCIR on Gemini South in Program GS-2001B-Q22. The observations were obtained on the nights of 2001 December 3, 5, and 9. The subsample was selected among those CTTs with $K_s < 11$ and with large excesses in the JHK_s diagram. OSCIR is a mid-IR ($8\text{--}25 \mu\text{m}$) imager and low/medium-resolution ($R = 100\text{--}1000$) spectrograph, which uses

⁵ IRAF is distributed by the National Optical Astronomy Observatory, which is operated by the Association of Universities for Research in Astronomy, Inc., under cooperative agreement with the National Science Foundation (NSF).

TABLE 1
OPTICAL AND NEAR-INFRARED PHOTOMETRY

CVSO	V	$B-V$	$U-V$	$V-R$	$V-I$	J	$J-H$	$H-K_s$	L
1.....	17.12	1.36	-0.36	1.26	2.81	12.82	0.68	0.25	...
3.....	16.31	1.47	0.99	1.06	2.25	12.69	0.67	0.26	...
5.....	16.09	1.48	0.81	1.08	2.23	12.50	0.68	0.22	...
10.....	15.41	1.42	1.27	0.93	1.91	12.31	0.68	0.24	...
11.....	15.74	1.53	0.96	1.08	2.33	12.10	0.66	0.23	...
15.....	15.95	1.44	0.46	0.90	2.12	12.57	0.74	0.19	...
17.....	16.16	1.51	...	1.07	2.34	12.52	0.72	0.20	...
19.....	15.89	1.49	1.54	1.14	2.51	11.92	0.69	0.21	...
22.....	16.33	1.51	0.86	1.06	2.29	12.70	0.66	0.22	...
24.....	16.31	1.49	...	1.06	2.25	12.79	0.72	0.14	...
25.....	15.46	1.42	...	0.95	1.91	12.42	0.69	0.15	...
29.....	16.25	1.51	...	1.14	2.53	12.38	0.67	0.24	...
34.....	15.15	1.36	1.16	0.96	1.97	12.28	0.99	0.23	...
34.....	15.15	1.36	1.16	0.96	1.97	12.72	1.34	0.23	...
35.....	14.55	1.41	0.73	0.99	1.95	11.46	0.70	0.41	...
	14.84	1.30	0.76	0.92	1.93	11.46	0.70	0.41	...
36.....	16.07	1.45	...	1.09	2.35	12.38	0.69	0.21	...
38.....	16.24	1.57	0.99	1.07	2.27	12.79	0.73	0.23	...
38.....	16.37	1.26	1.12	1.07	2.46	12.79	0.73	0.23	...
39.....	15.98	1.41	0.90	1.07	2.45	12.30	0.68	0.20	...
39.....	16.11	1.22	0.66	1.10	2.46	12.30	0.68	0.20	...
40.....	15.23	1.35	1.07	0.90	1.81	12.36	0.72	0.26	...
41.....	15.23	0.97	0.28	0.73	1.54	12.41	0.70	0.33	...
42.....	15.96	1.43	1.12	1.03	2.15	12.68	0.68	0.17	...
43.....	16.27	1.42	0.98	1.09	2.46	12.50	0.74	0.16	...
44.....	14.74	1.21	0.96	0.73	1.43	12.30	0.66	0.08	...
46.....	15.15	1.42	...	0.94	1.93	12.02	0.69	0.21	...
46.....	15.19	1.46	0.91	0.94	1.92	12.02	0.69	0.21	...
47.....	15.09	1.38	1.12	0.93	1.86	11.28	0.84	0.50	9.36
48.....	14.07	1.16	0.70	0.78	1.44	11.50	0.68	0.22	10.45
54.....	15.80	1.31	1.18	0.91	1.95	12.86	0.70	0.14	...
55.....	15.60	1.43	1.16	1.06	2.27	11.93	0.69	0.24	...
55.....	15.69	1.54	0.99	1.01	2.26	11.93	0.69	0.24	...
57.....	15.67	0.91	1.91	12.65	0.72	0.19	...
58.....	14.93	0.89	-0.30	0.84	1.65	12.05	0.78	0.56	9.97
72.....	17.98	1.64	0.87	0.94	2.22	14.49	0.71	0.21	...
75.....	16.72	0.92	0.41	0.44	1.04	13.00	0.76	0.51	...
77.....	16.37	1.42	...	1.07	2.26	12.81	0.72	0.23	...
81.....	16.22	1.45	0.87	1.17	2.54	12.24	0.66	0.23	...
90.....	14.61	0.38	-0.97	0.65	1.40	12.13	0.91	0.67	9.73
104.....	14.22	0.79	-0.08	0.66	1.44	11.78	0.75	0.58	...
107.....	14.78	0.84	-0.38	0.81	1.73	11.55	0.81	0.45	9.85
109.....	13.97	0.88	-0.35	0.80	1.69	11.01	0.80	0.42	9.37
121.....	14.24	1.18	0.23	0.87	1.69	11.70	0.92	0.64	...
124.....	15.91	1.50	0.89	1.11	2.41	12.07	0.70	0.25	...
126.....	15.82	1.44	0.99	0.92	1.85	12.85	0.71	0.17	...
133.....	14.88	1.15	1.01	0.76	1.59	12.19	0.61	0.15	...
143.....	15.25	1.34	0.41	1.03	2.19	11.79	0.78	0.21	...
146.....	13.92	1.19	0.14	0.84	1.63	11.30	0.86	0.42	9.65
	14.01	1.52	11.30	0.86	0.42	9.65
152.....	13.98	1.12	0.81	0.71	1.40	11.58	0.82	0.50	...
153.....	16.00	1.43	-0.64	1.07	2.29	12.44	0.72	0.23	...
155.....	14.35	1.33	0.63	0.92	1.85	11.48	0.66	0.33	...
157.....	17.87	0.70	-0.98	1.14	2.09	14.01	0.59	0.35	...
164.....	16.71	1.55	0.30	1.31	3.03	11.80	0.69	0.32	...
165.....	13.68	1.12	0.45	0.76	1.48	11.07	0.83	0.41	9.24
168.....	17.33	1.24	-0.25	1.27	2.82	12.78	0.60	0.28	...
171.....	14.84	1.46	0.64	0.84	1.69	11.96	0.70	0.30	...
176.....	15.65	1.21	-0.35	1.14	2.46	11.71	0.91	0.50	9.84
177.....	15.62	0.71	...	0.96	1.92	12.30	0.77	0.33	10.98
178.....	15.66	1.48	0.64	1.11	2.28	11.47	0.77	0.34	...
181.....	15.63	1.22	...	0.87	2.00	12.30	0.74	0.19	...
184.....	15.34	1.86	...	1.41	2.75	10.40	1.27	0.91	...
185.....	15.28	1.61	...	1.08	2.18	10.88	0.88	0.49	8.77
190.....	14.04	1.10	0.28	0.83	1.72	11.04	1.08	0.77	8.49
	14.76	1.89	11.04	1.08	0.77	8.49
192.....	15.99	1.26	-0.14	1.17	2.37	11.56	1.01	0.55	99.00
193.....	15.15	1.29	0.04	1.15	2.29	11.34	1.22	0.66	99.00

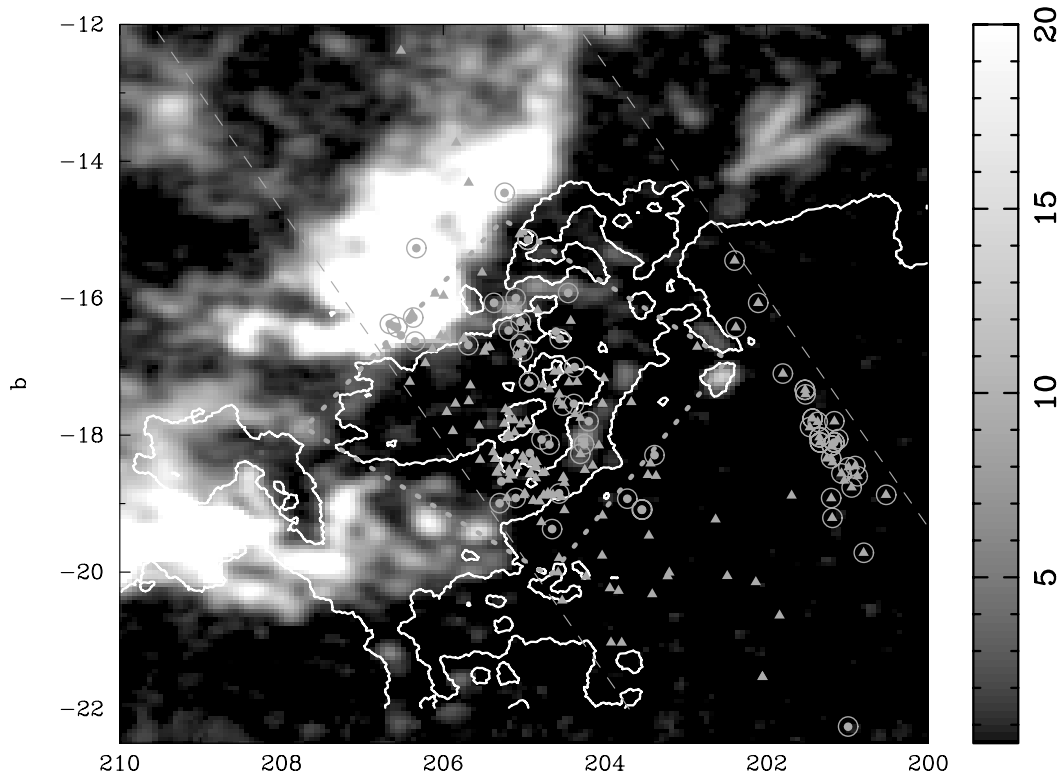
TABLE 2
OSCIR PHOTOMETRY

CVSO	N	Error N	18 μm	Error 18 μm	$\log \lambda F_{\lambda}(N)$ $\log (\text{ergs s}^{-1} \text{cm}^{-2})$	$\log \lambda F_{\lambda}(18 \mu\text{m})$ $\log (\text{ergs s}^{-1} \text{cm}^{-2})$
47.....	9.418	0.081	>7.627	0.383	-11.779 ± 0.03	<-11.654
58.....	8.448	0.388	>7.517	0.444	-11.391 ± 0.15	<-11.576
90.....	8.294	0.282	>9.533	2.773	-11.330 ± 0.12	<-11.792
107....	8.109	0.276	>9.092	1.866	-11.256 ± 0.12	<-11.764
109....	7.935	0.120	6.437	0.165	-11.186 ± 0.05	-11.492 ± 0.1
165....	6.921	0.093	>6.983	0.279	-10.781 ± 0.05	<-11.710

a 128×128 pixel Si:As IBC detector optimized for the wavelength range $8\text{--}25 \mu\text{m}$. On Gemini, OSCIR has a plate scale of about $0''.084 \text{ pixel}^{-1}$ and a total field of view in its imaging configuration of $11'' \times 11''$. We used the N -wide filter ($\lambda_{\text{eff}} = 10.8 \mu\text{m}$ and $\Delta\lambda = 5.23 \mu\text{m}$) and the IHW18 filter ($\lambda_{\text{eff}} = 18.2 \mu\text{m}$ and $\Delta\lambda = 1.65 \mu\text{m}$). In the rest of this article we refer to these filters as the 10 and 18 μm filters. Typical exposure times for the Orion targets were 60 s at 10 μm and 300 s at 18 μm . Sky conditions were mostly clear through the observations. All the observations were performed using the standard technique of chopping and nodding, with a chop throw of $15''$ in declination. For calibration of the photometry the standard star α CMa (Sirius) was observed on all nights at both wavelengths. Flux density estimates for Sirius were calculated using the spectral energy distributions (SEDs) published by Cohen et al. (1999). For Sirius, integration times were on the order of 6 s in both 10 and 18 μm . The data were processed through the standard pipeline for OSCIR data. Chop

pairs are subtracted: beam A – beam B or beam B – beam A for each set, depending on the nod position. Then these differences are averaged to form a final image. Because we were dealing with point sources, per recommendation of the Gemini staff no flat fielding was performed. The OSCIR array is very flat over the small number of pixels within the point-spread function. Experience shared between Gemini and University of Florida is that the errors associated with the photometric calibration ($\sim 10\%$) are much larger than any flat-field correction.

The 10 and 18 μm images showed only one object per frame, when detected at all. We used APPHOT to obtain aperture photometry of all targets. Images at 10 μm showed typical FWHM ~ 6 pixels (or $\sim 0''.5$), so we used an aperture radius of 15 pixels and inner and outer sky annulus radii of 15 and 25 pixels, respectively. Because most of the Orion stars were not detected at 18 μm , we used consecutive pairs of 10 and 18 μm α CMa images to determine average offset positions between the two filters and to place



1

FIG. 1.—Galactic coordinates of the stars in the photometric sample (*big open circles*) compared to the Orion Variability Survey sample of Paper I (CTTSs, *filled circles*; WTTS, *triangles*). The integrated ^{13}CO emissivity from Bally et al. (1987) is shown in a half-tone gray scale, covering the range from 0.5 to 20 K km s^{-1} . The isocontour for $A_V = 1$ from Schlegel et al. (1998) is also shown. The dotted lines show the boundaries of Ori OB1b adopted in Paper I and this work. The dashed lines show the limits of the survey in Paper I.

TABLE 3
STELLAR AND ACCRETION PROPERTIES

CVSO	Spectral Type	T_{eff} (K)	L (L_{\odot})	R (R_{\odot})	M (M_{\odot})	A_V	Age (Myr)	L_{acc} (L_{\odot})	\dot{M} ($10^{-8} M_{\odot} \text{ yr}^{-1}$)	Association	Type
1.....	M3	3470	0.18	1.17	0.33	0.81	4.02	0.01	0.09	1a	CTTS
3.....	M3	3470	0.16	1.11	0.33	0.00	4.68	0.00	0.00	1a	WTTS
5.....	M2	3580	0.21	1.20	0.38	0.22	4.12	0.00	0.01	1a	WTTS
10.....	M0	3850	0.27	1.17	0.58	0.27	7.20	0.00	0.00	1a	WTTS
11.....	M2	3580	0.33	1.49	0.39	0.46	2.51	0.00	0.02	1a	WTTS
15.....	M1	3720	0.21	1.11	0.47	0.39	6.42	0.00	0.03	1a	WTTS
17.....	M3	3470	0.19	1.20	0.33	0.00	3.63	0.00	0.06	1a	WTTS
19.....	M3	3470	0.34	1.60	0.34	0.10	2.23	1a	WTTS
22.....	M2	3580	0.18	1.12	0.38	0.36	5.18	0.00	0.01	1a	WTTS
24.....	M2	3580	0.17	1.06	0.38	0.27	5.97	0.00	0.01	1a	WTTS
25.....	M0	3850	0.24	1.11	0.58	0.27	8.09	1a	WTTS
29.....	M2	3580	0.29	1.40	0.39	0.94	2.73	1a	WTTS
34.....	M0	3850	0.29	1.21	0.58	0.41	6.61	0.00	0.01	1a	WTTS
34.....	M0	3850	0.19	0.98	0.59	0.41	10.55	0.00	0.01	1a	WTTS
35.....	K7	4060	0.72	1.72	0.77	0.85	2.88	0.02	0.17	1a	CTTS
	K7	4060	0.71	1.70	0.77	0.80	2.90	0.02	0.13	1a	CTTS
36.....	M3	3470	0.21	1.28	0.34	0.00	2.95	0.03	0.36	1a	WTTS
38.....	M2	3580	0.17	1.06	0.38	0.31	5.88	0.00	0.00	1a	WTTS
38.....	M2	3580	0.19	1.13	0.38	0.77	4.98	0.00	0.02	1a	WTTS
39.....	M2	3580	0.30	1.41	0.39	0.74	2.70	0.00	0.04	1a	WTTS
39.....	M2	3580	0.30	1.42	0.39	0.77	2.68	0.01	0.08	1a	WTTS
40.....	M0	3850	0.24	1.10	0.58	0.02	8.18	0.00	0.00	1a	CTTS
41.....	K2	4900	0.37	0.84	0.89	1.30	88.18	0.06	0.19	1a	CTTS
42.....	M2	3580	0.17	1.08	0.38	0.02	5.71	0.00	0.00	1a	WTTS
43.....	M2	3580	0.25	1.29	0.39	0.77	3.03	0.00	0.02	1a	WTTS
44.....	K6	4205	0.27	0.98	0.82	0.00	22.97	0.00	0.01	1a	WTTS
46.....	M0	3850	0.36	1.34	0.58	0.32	4.74	0.00	0.03	1a	WTTS
46.....	M0	3850	0.35	1.34	0.58	0.29	4.80	0.00	0.02	1a	WTTS
47.....	K5	4350	0.97	1.73	1.10	1.21	4.96	0.01	0.04	1a	CTTS
48.....	K4	4590	1.25	1.77	1.28	0.71	6.60	0.05	0.22	1b	CTTS
54.....	M0	3850	0.17	0.92	0.58	0.36	14.57	0.00	0.01	1a	WTTS
55.....	M2	3580	0.37	1.58	0.39	0.31	2.30	0.00	0.01	1a	WTTS
55.....	M2	3580	0.37	1.58	0.39	0.29	2.31	0.00	0.01	1a	WTTS
57.....	M0	3850	0.20	1.00	0.59	0.27	9.95	0.00	0.00	1a	CTTS
58.....	K7	4060	0.61	1.58	0.78	0.12	4.02	0.07	0.45	1b	CTTS
72.....	M6	3050	0.04	0.74	0.11	0.00	6.20	0.00	0.01	1b	CTTS
75.....	M1	3720	0.23	1.16	0.47	0.00	5.82	0.00	0.04	1b	CTTS
77.....	K6	4205	0.28	0.99	0.82	1.88	21.91	1a	WTTS
81.....	M3	3470	0.45	1.86	0.34	0.17	1.76	0.00	0.02	1b	WTTS
90.....	K7	4060	0.55	1.50	0.79	0.00	5.04	0.29	1.77	1b	CTTS
104.....	K7	4060	0.76	1.76	0.77	0.00	2.76	0.10	0.75	1b	CTTS
107.....	K7	4060	1.02	2.04	0.77	0.32	2.12	0.13	1.09	1b	CTTS
109.....	M0	3850	1.48	2.73	0.56	0.00	0.80	0.16	2.52	1b	CTTS
121.....	K3	4730	1.31	1.70	1.32	1.49	8.06	0.40	1.67	1b	CTTS
124.....	M3	3470	0.51	1.97	0.34	0.00	1.58	0.00	0.02	1b	WTTS
126.....	M0	3850	0.16	0.89	0.58	0.12	16.16	0.00	0.00	1a	WTTS
133.....	K6	4205	0.32	1.06	0.84	0.27	18.14	0.00	0.01	1a	WTTS
143.....	M1	3720	0.82	2.18	0.47	0.55	1.16	0.02	0.37	1b	CTTS
146.....	K6	4205	1.32	2.17	0.91	0.37	2.01	0.11	0.81	1b	CTTS
	K6	4205	1.23	2.09	0.92	0.10	2.19	0.12	0.88	1b	CTTS
152.....	K3	4730	1.21	1.64	1.30	0.78	8.65	0.03	0.14	1b	CTTS
153.....	M2	3580	0.23	1.26	0.39	0.36	3.43	0.02	0.16	1a	WTTS
155.....	K6	4205	1.30	2.14	0.91	0.90	2.06	0.07	0.53	1b	CTTS
157.....	C	1b	CTTS
164.....	M3	3470	1.06	2.85	0.35	1.82	0.45	0.05	1.19	1b	CTTS
165.....	K6	4205	1.48	2.29	0.91	0.00	1.72	0.05	0.37	1b	CTTS
168.....	M4	3370	0.25	1.46	0.29	0.00	2.49	0.00	0.05	1b	CTTS
171.....	K5	4350	0.82	1.60	1.08	0.81	6.41	0.02	0.10	1b	CTTS
176.....	M3	3470	0.71	2.32	0.35	0.00	1.06	0.02	0.43	1b	CTTS
177.....	K6	4205	0.64	1.50	0.94	1.07	6.21	0.01	0.04	1b	CTTS
178.....	M1	3720	1.17	2.60	0.47	0.77	0.81	0.01	0.25	1b	CTTS
181.....	M0	3850	0.51	1.61	0.57	0.48	2.63	0.02	0.14	1b	CTTS

TABLE 3—Continued

CVSO	Spectral Type	T_{eff} (K)	L (L_{\odot})	R (R_{\odot})	M (M_{\odot})	A_V	Age (Myr)	L_{acc} (L_{\odot})	\dot{M} ($10^{-8} M_{\odot} \text{ yr}^{-1}$)	Association	Type
184.....	K1	5080	9.67	4.01	2.35	4.35	2.03	1b	CTTS
185.....	K7	4060	2.54	3.22	0.81	1.40	0.79	1b	CTTS
190.....	K6	4205	1.78	2.52	0.90	0.58	1.26	0.13	1.17	1b	CTTS
	K6	4205	1.99	2.66	0.90	0.99	1.00	0.14	1.38	1b	CTTS
192.....	K6	4205	1.68	2.44	0.90	2.14	1.40	0.36	3.08	1c	CTTS
193.....	K6	4205	1.96	2.63	0.90	1.95	1.02	0.48	4.49	1c	CTTS

the aperture at the predicted position in the $18 \mu\text{m}$ images of the Orion stars. In this way we measured upper limits to the flux in this band.

The mid-IR measurements are listed in Table 2. All stars were detected at $10 \mu\text{m}$, but only one measurement was secured at $18 \mu\text{m}$. We list 3σ upper limits in Table 2 for the nondetections.

3. RESULTS

3.1. Environment of the Sample

The Galactic coordinates of stars in the photometric sample are plotted in Figure 1 compared with the entire sample in Paper I. The stars are projected against the map of integrated ^{13}CO emissivity from Bally et al. (1987). It can be seen that our sample is representative of that in Paper I. It includes the CTTSs and a number of WTTSs in the “clump” at ($l = 202^\circ$, $b = -18^\circ$) in Ori OB1a. It also includes a number of CTTSs in Ori OB1b, located mostly inside of the molecular ring of higher extinction (cf. Paper I). Some of these stars are probably associated with NGC 2023 and NGC 2024. Here we adopt the boundaries of Ori OB1b from Paper I, shown in Figure 1. However, there is some uncertainty in the actual membership of stars located near the assumed boundary

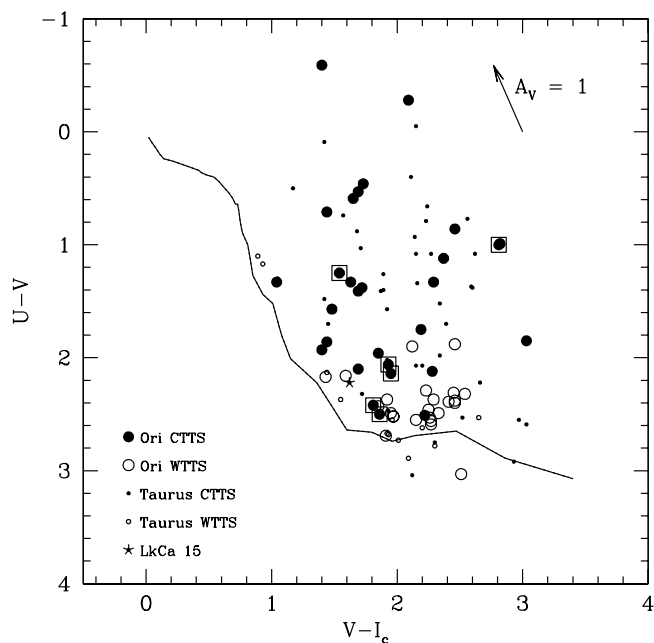


FIG. 2.—Location of the stars in the $U - V$ vs. $V - I_c$ diagram. We show the CTTSs (filled large circles), and WTTSs (open large circles) for the Ori OB1 sample, with the stars in Ori OB1a in open rectangles. The Taurus CTTSs (small filled circles), WTTSs (small open circles), and the sequence for dwarf standards from KH95 are also shown, as well as the reddening vector for $A_V = 1$ calculated with the Cardelli et al. (1989) reddening law for $R_V = 3.1$. The star corresponds to the Taurus CTTS LkCa 15.

between Ori OB1a and 1b at $l \sim 203^\circ 7$, $b \sim -18^\circ$ to -19° . In addition, with the adopted boundaries, two stars of the sample fall in Ori OB1c, in the region of high molecular gas density; however, they are so close to the uncertain boundary that we include them in Ori OB1b for the rest of the analysis.

3.2. Stellar Properties

We took the spectral types of the sample stars from Paper I and recalculate here stellar properties from the simultaneous multiwavelength photometry to minimize effects of variability. We used the average distances of 330 pc for Ori OB1a and 440 pc for Ori OB1b, as discussed in Paper I. The extinctions A_V in Table 3 are calculated from the $V - I_c$ color, using the Cardelli et al. (1989) extinction law with $R_V = 3.1$. The mean extinctions for Ori OB1a, 1b, 1c, and the entire sample are 0.5, 0.6, 2, and 0.6 mag, respectively. Using individual extinctions, we recalculated stellar luminosities L and radii R . Location in the H-R diagram and comparison with the Siess et al. (2000) tracks yielded stellar masses M and ages. These quantities, shown in Table 3, in general agree within 50% with those of Paper I.

3.3. Color-Color Diagrams

Figures 2 and 3 show photometry from Table 1 plotted in the $U - V$ versus $V - I_c$ and $U - B$ versus $V - I_c$ diagrams, as well as the location of the main-sequence colors taken from Kenyon &

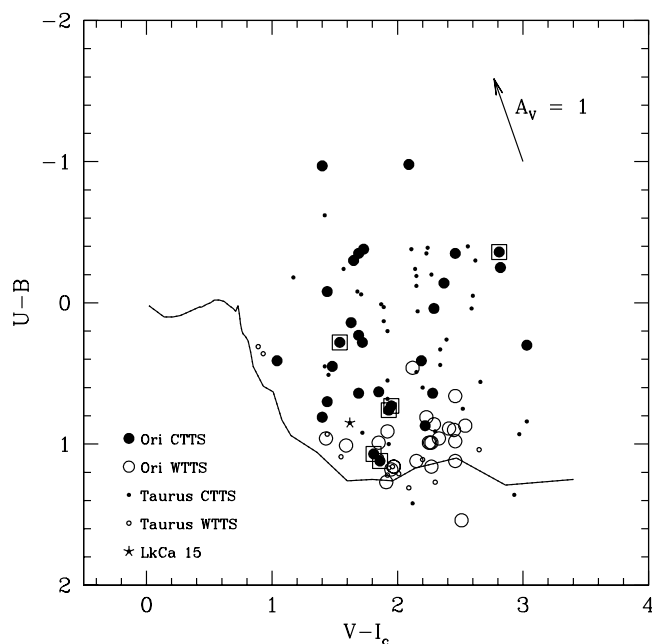


FIG. 3.—Location of the stars in the $U - B$ vs. $V - I_c$ diagram. Symbols are as in Fig. 2.

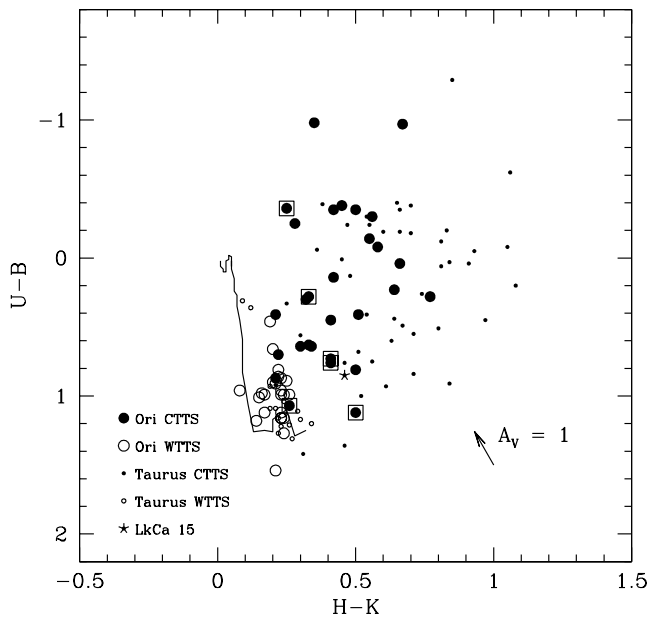


FIG. 4.—Location of the stars in the $U - B$ vs. $H - K$ diagram. Symbols are as in Fig. 2. The $H - K$ colors for the Ori OB1 stars are from the 2MASS survey, corrected to the CIT system.

Hartmann (1995, hereafter KH95). CTTSs and WTTSs are shown separately, and the CTTSs in Ori OB1a are marked. Note that the two observations for stars CVSO 35, 146, and 190 are plotted as different points.

The WTTSs in the sample are consistent with main-sequence colors, reddened by ~ 0.5 – 0.6 mag of extinction, as expected from the average A_V of the sample. The CTTSs have similar $V - I_C$ as the WTTSs but show large excesses relative to the WTTSs in $U - V$ and $U - B$. These excesses are expected to arise from emission of the accretion shock formed as material accreting from the disk strikes the stellar surface (Hartigan et al. 1991, 1995; Calvet & Gullbring 1998).

In Figures 2 and 3 we also plot a sample of stars in Taurus taken from KH95, equally separated in WTTSs and CTTSs. The age of the Taurus association has been analyzed in detail by Hartmann (2003), who showed that most of the stars have ages of ~ 1 – 2 Myr. With the ages for the subassociations found in Paper I, i.e., ~ 3 – 5 Myr for Ori OB1b and ~ 7 – 10 Myr for OB1a, the Taurus population is younger than Ori OB1b by ~ 2 – 3 Myr and than Ori OB1a by ~ 6 – 8 Myr, so it provides an initial reference point to study evolutionary effects.

The Orion OB1 and Taurus stars encompass a similar range of $V - I_C$ in Figures 2 and 3, indicating that we are probing the same range of stellar masses. The samples of Ori OB1b and Taurus show a similar range in $U - V$ and $U - B$ excesses relative to photospheric colors; the lowest excesses correspond to stars in Ori OB1a, some of them compatible with measurements for the WTTSs.

In Figure 4 we show the Ori OB1 sample in the $U - B$ versus $H - K$ diagram, indicating the standard main-sequence colors with values from KH95. We have used the transformations from Carpenter (2001) to convert the 2MASS $H - K_s$ colors to the CIT system. A sample of Taurus stars, with colors from KH95, is also shown. It is apparent that the excesses in $H - K$ relative to photospheric colors in Ori OB1b are smaller than those found in the Taurus sample. Moreover, the excesses in $H - K$ in Ori OB1a, the oldest of the three populations shown, are even smaller than in Ori OB1b.

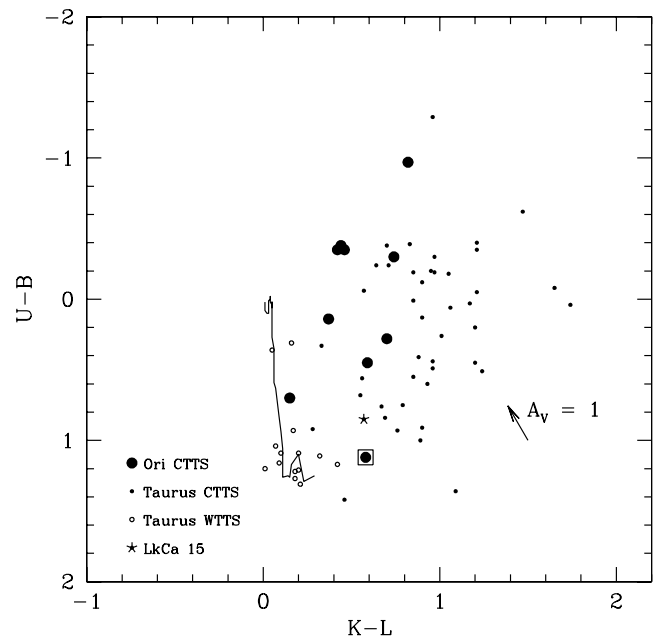


FIG. 5.—Location of the stars in the $U - B$ vs. $K - L$ diagram. Symbols are as in Fig. 2.

This effect is more apparent in the $U - B$ versus $K - L$ diagram, shown in Figure 5, using the $K - L$ colors of the CTTSs in Ori OB1 in Table 1. We use here K_s for the Orion OB1 stars. Colors for the Taurus stars and for the main sequence are from KH95. The color excesses in $K - L$ relative to the main sequence in the Ori OB1 stars are clearly smaller than those in Taurus.

Finally, we locate the six stars observed with Gemini OSCIR in the $K - L$ versus $K - N$ diagram in Figure 6 and compare them to the Taurus sample. The Ori OB1 stars are located at the low end of the Taurus CTTS distribution and even tend to populate the clear gap between CTTSs and WTTSs noticed by KH95. (The three Taurus stars inside the gap are binaries [KH95].)

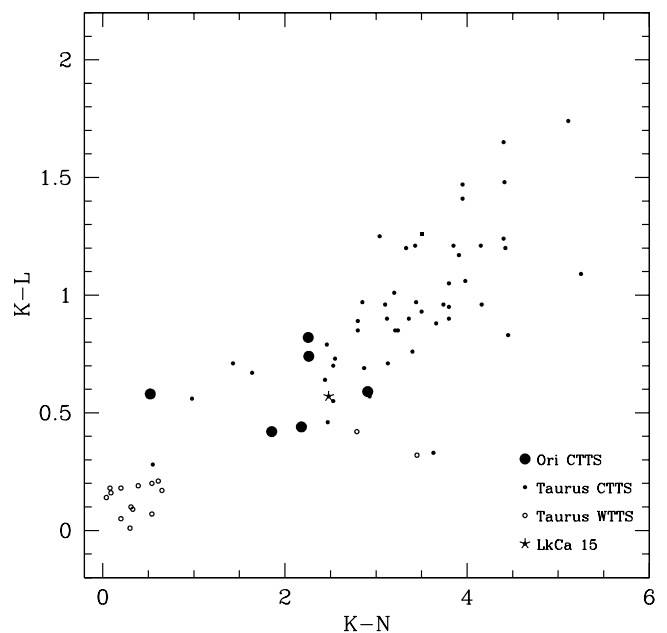


FIG. 6.—Location of the stars in the $K - L$ vs. $K - N$ diagram. Symbols are as in Fig. 2.

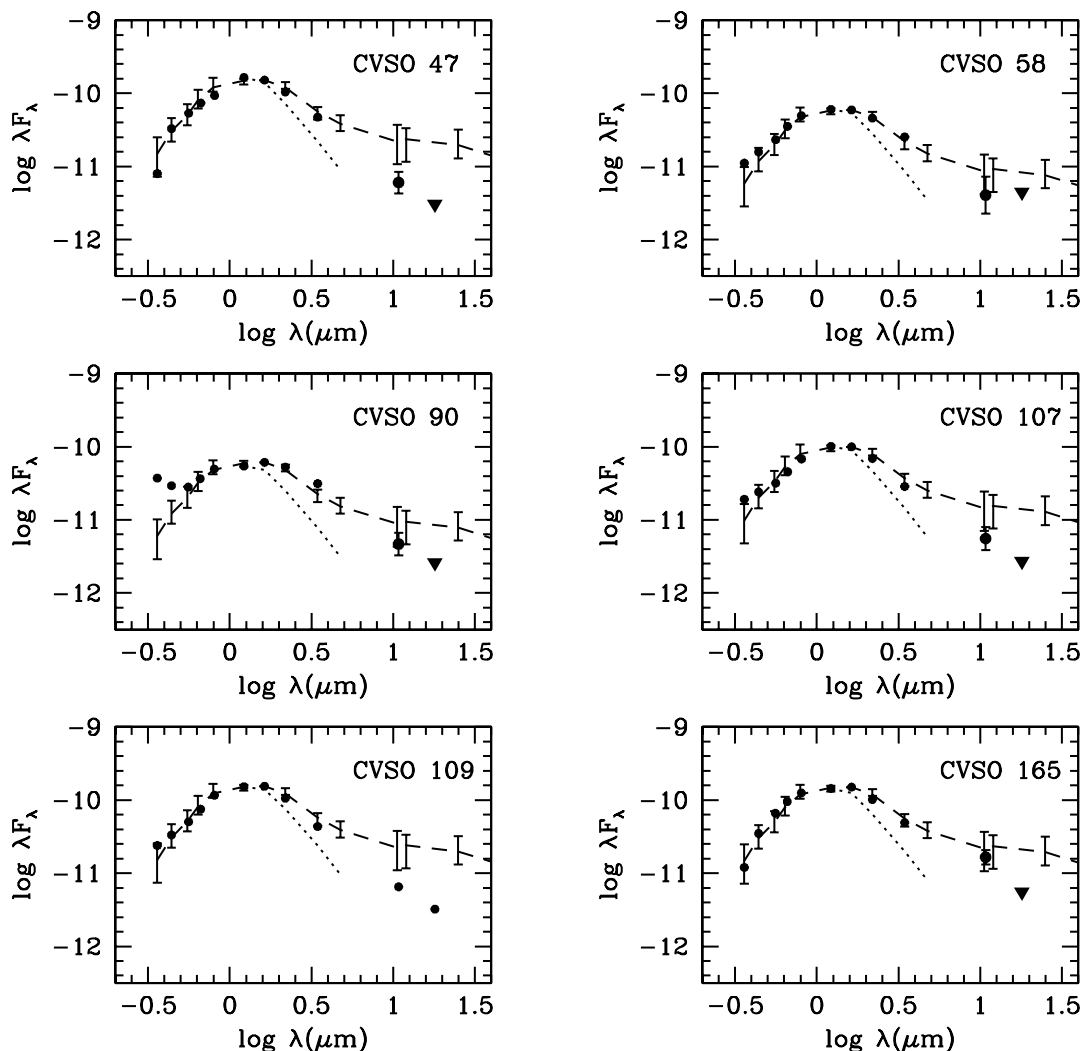


FIG. 7.—SEDs of stars observed with Gemini OSCIR (circles) compared with the Taurus median (D01; dashed lines), normalized to the H magnitude of each star. The error bars in the Taurus median correspond to the first quartiles. The triangles indicate upper limits. The photospheric fluxes in the near-IR (dotted lines) are constructed from colors of dwarfs from KH95, normalized to the H magnitude of each star.

These comparisons clearly indicate a decrease of IR emission at $\leq 10 \mu\text{m}$ with age. A significant decrease of $H - K$ and $K - L$ with age is also found in a sample of clusters and groupings by Hillenbrand et al. (2005, in preparation), and Sicilia-Aguilar et al. (2005) observe a similar near-IR flux deficit relative to Taurus in *Spitzer* IRAC colors of the ~ 5 Myr cluster Tr 37. IR emission shortward of $10 \mu\text{m}$ arises in the inner disks, inward of a few AU, in T Tauri stars, which are sufficiently hot to produce such emission (Meyer et al. 1997; D’Alessio et al. 1998, 1999, 2001). Thus, the observed decrease of fluxes with age must be related to physical phenomena occurring in these inner regions of the disks as a result of disk evolution. We explore possible implications of these results in § 4.

3.4. Spectral Energy Distributions

Analyses of color-color diagrams in § 3.3 indicate a clear difference between emission of the disks in Ori OB1 and in Taurus; disks in the Orion OB1 stars emit less flux at near-IR wavelengths than typical disks in Taurus. The comparison is seen clearly in Figure 7, where we plot the SEDs of the stars observed with Gemini OSCIR, including the measurement and upper limits at $18 \mu\text{m}$ from Table 2. Optical and near-IR fluxes have been calculated from magnitudes in Table 1 and corrected

for reddening in Table 3. These SEDs are compared with the median SED of CTTSs in Taurus (D’Alessio et al. 2001, hereafter D01), scaled to the flux at H of each star. The error bars in the median show the first quartiles of the distribution (i.e., 50% of the Taurus stars fall within the error bars).

The SEDs of the Orion stars show excesses relative to the photosphere, consistent with the fact that the sample observed with Gemini was selected on the basis of being bright at K and having large $H - K$ excesses. However, even with this selection bias, the Ori OB1 disks are fainter than $\sim 50\%$ – 75% of the Taurus sample in the mid-IR.

3.5. Mass Accretion Rates

We interpret the excesses in $U - B$ and $U - V$ relative to photospheric fluxes in the CTTSs in Ori OB1a and 1b as due to emission from the accretion shock on the stellar surface (Hartigan et al. 1991, 1995; Gullbring et al. 1998; Calvet & Gullbring 1998). In the framework of this interpretation, the excess luminosity above photospheric colors is a measure of the accretion luminosity released as matter falls from the disk onto the star, following the magnetic field lines that disrupt the disk (cf. Hartmann 1998). We used the dereddened U photometry and spectral types to obtain the excess luminosity in U above the intrinsic

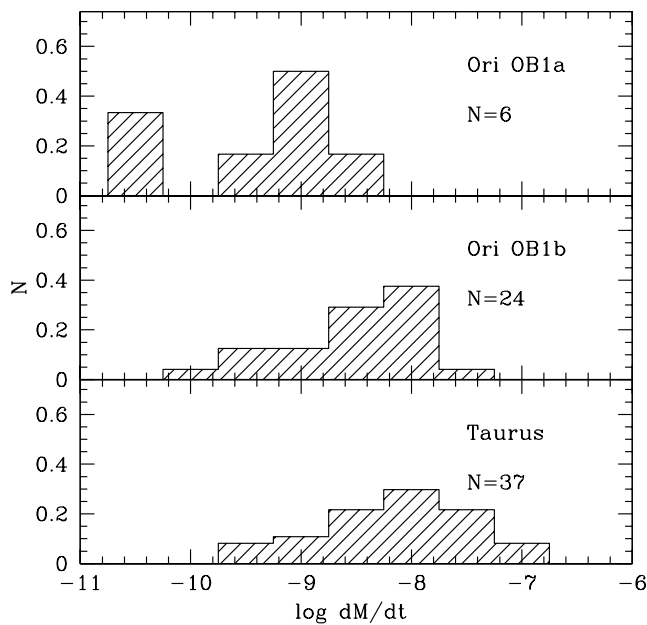


FIG. 8.—Distribution of mass accretion rates for Ori OB1a (top), Ori OB1b (middle) and Taurus (bottom). Data from Taurus from Gullbring et al. (1998) and Hartmann et al. (1998) are recalculated with masses estimated from the Siess et al. (2000) evolutionary tracks.

photospheric fluxes, L_U ; this luminosity was used to estimate the accretion luminosity, L_{acc} , using the calibration of Gullbring et al. (1998). These estimates are listed in Table 3. The largest uncertainty in the determination of L_U , and thus L_{acc} , comes from uncertainties in the determination of the extinction A_V , which amount to $\sim 30\%$ – 40% .

Using $L_{acc} \sim 0.8GM\dot{M}/R_*$ (assuming a radius of $\sim 5R_*$ for the magnetospheric radius; Calvet & Gullbring 1998), with the mass and radius determined from the location in the H-R diagram, we can infer the mass accretion rate \dot{M} of the objects. These rates are listed in Table 3. In addition to the uncertainties in L_{acc} , the formal uncertainty in \dot{M} includes errors in radius and mass, which are of order 15%–20%; thus, the mass accretion rates are constrained within a factor of 2. Given the uncertainties in the original calibration between L_U and L_{acc} , this uncertainty can be a factor of 2 larger (Gullbring et al. 1998). As the errors are uncorrelated, the total error amounts to a factor of 3.

In Figure 8 we show histograms with the number of objects per bin of $\log \dot{M}$, each of size 0.5, for the three populations, with Ori OB1a at the top, 1b at the middle, and Taurus at the bottom. The mass accretion rates in Taurus are taken from Gullbring et al. (1998) and Hartmann et al. (1998). These measurements of \dot{M} were obtained from L_{acc} using masses estimated with the D’Antona & Mazzitelli (1994) evolutionary tracks; we have recalculated them using masses for the Taurus stars estimated with the Siess et al. (2000) evolutionary tracks, for consistency with the work presented here. The actual values of \dot{M} in bins with $\dot{M} < 10^{-10} M_\odot \text{ yr}^{-1}$ are highly uncertain. At these levels, emission due to stellar surface activity becomes an important or dominant contributor to the U excess, as comparison with the WTTSs in the sample shows. In these cases, the determined values are upper limits to the true \dot{M} s.

The age of the three populations shown increases from bottom to top. In all three cases, there is a large spread in the ranges of values of \dot{M} . However, as time proceeds, the number of rapid accretors decreases; only the low accretors remain in Ori OB1a. One “continuum” star is found in Ori OB1b (see Table 3); we did

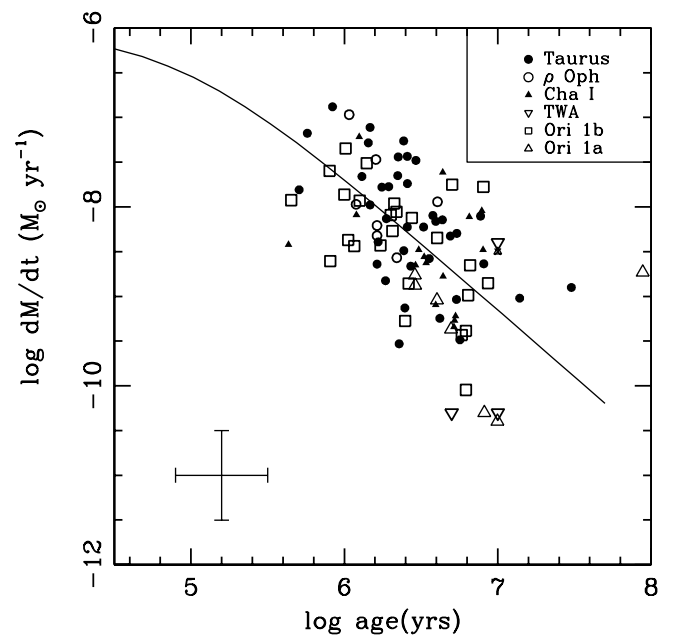


FIG. 9.—Mass accretion rate vs. age for several associations: Ori OB1a (open upward-pointing triangles), Ori OB1b (squares), Taurus (filled circles), ρ Oph (open circles), Chamaeleon I (filled triangles), TWA (open downward-pointing triangles), with data from Hartmann et al. (1998) and Muzerolle et al. (2000, 2001). The solid line shows a model for viscous evolution for an initial disk mass of $0.2 M_\odot$ and $\alpha = 0.01$ from Hartmann et al. (1998). A typical error bar is shown.

not have enough spectral resolution to distinguish spectral features and thus determine its spectral type and derived properties. This continuum star does not appear in Figure 8; if its properties were similar to those of continuum stars in Taurus, then it could have $\dot{M} \sim \text{few} \times 10^{-7} M_\odot \text{ yr}^{-1}$ (Gullbring et al. 1998, 2000; Calvet & Gullbring 1998). However, even including this star, the relative number of rapid accretors in Ori OB1b would be smaller than in Taurus.

We compared the distributions of $\log \dot{M}$ in the three regions using a two-sided K-S test. The results indicated that the probability that the Ori OB1b and Taurus samples are drawn from the same underlying distribution is only 3%; the same is true for Ori OB1b versus Ori OB1a. For a further test, we have added the continuum star in Ori OB1b to the distribution, assuming a mass accretion rate of $10^{-7} M_\odot \text{ yr}^{-1}$; even in this case, the probability that the Ori OB1b sample is drawn from the same distribution as Taurus is only marginally larger, 9%. Thus, we conclude that the distributions of accretion rates are significantly different between the three regions.

Figure 9 plots the derived mass accretion rates and ages of CTTs in Ori OB1a and 1b from Table 3. We also plot in Figure 9 similar data for Taurus, ρ Oph, Chameleon (Hartmann et al. 1998), and the TW Hya association (TWA; Muzerolle et al. 2000). All masses and mass accretion rates of these latter objects have been recalibrated using the Siess et al. (2000) evolutionary tracks. The mass accretion rates of the disks in Ori OB1 are consistent with those in other associations and show a clear decrease with age. The star CVSO 41 in Ori OB1a has an apparent age of 88 Myr (Table 3) and still shows a fairly high value of \dot{M} . The spectral type of this star is K2, so it could have a large age uncertainty. It is known that pre-main-sequence stars in this spectral type range tend to have higher apparent ages than cooler objects (Hillenbrand 1997); this behavior has been attributed to uncertainties in the birth line location (Hartmann 2003).

The solid line in Figure 9 shows the decay of \dot{M} with time expected from viscous evolution for a disk with initial mass $0.2 M_{\odot}$ and viscous parameter $\alpha = 0.01$, from Hartmann et al. (1998). The new values of \dot{M} help confirm a decrease of \dot{M} with age qualitatively consistent with viscous disk evolution. However, viscous evolution cannot explain the decreasing fraction of accreting objects with age (Muzerolle et al. 2000; Briceño et al. 2005); other factors (i.e., inner disk clearing associated with planet formation; Calvet et al. 2002; Rice et al. 2003) must play a role in slowing accretion onto the central star.

4. DISCUSSION

In our comparison of disk properties in three populations with ages $\sim 1\text{--}2$ Myr (Taurus), $3\text{--}5$ Myr (Ori OB1b), and $7\text{--}10$ Myr (Ori OB1a), we have found a clear decrease of disk emission with age. This decrease is apparent at all wavelengths with expected substantial disk contribution to the emission, from H to $18 \mu\text{m}$.

The disk emission in the IR depends on the temperature of the dust. The two main heating mechanisms active on disks around young stars are viscous dissipation and stellar irradiation (Kenyon & Hartmann 1987; D'Alessio et al. 1998, 1999, D01). Viscous dissipation depends on the mass accretion rate throughout the disk; for the range of stellar parameters of stars in Ori OB1, and for $\dot{M} \leq 10^{-8} M_{\odot} \text{ yr}^{-1}$, which characterizes these stars (§ 3.5), viscous heating is important only near the midplane of the innermost disk, ≤ 1 AU (D'Alessio et al. 1999, D01). Thus, absorption of stellar radiation by dust in the disks around the Ori OB1 stars mostly determines their temperature and emission.

One important development in recent years is the recognition that the near-IR fluxes in accretion disks around pre-main-sequence stars are dominated by emission from a sharp transition between dust and gas at the dust destruction radius. At this transition, the optically thick dust disk is high enough to form a “wall,” which is frontally illuminated by the star. Opacities in the inner gas disk are due to molecules and are much lower than the dust opacities for typically low mass accretion rates; thus, the gas disk is optically thin, enabling frontal illumination of the wall (Muzerolle et al. 2005). The existence of this wall was proposed for Herbig Ae/Be stars (Natta et al. 2001; Tuthill et al. 2001; Dullemond et al. 2001) to explain the peculiar “bump” at $\sim 3 \mu\text{m}$ observed in the SEDs of these stars (Hillenbrand et al. 1992). Interferometric measurements of inner disk structures in Herbig Ae/Be stars confirmed this prediction (Millan-Gabet et al. 1999; Monnier & Millan-Gabet 2002). A similar wall emission was then reported in the low-mass CTTSs by Muzerolle et al. (2003). In contrast to their higher mass counterparts, CTTSs can have accretion luminosities of the same order as the stellar luminosities, thus increasing the total energy output and moving outward the disk location where the temperature is equal to the dust destruction temperature for objects with high values of L_{acc} . The rapid accretors are therefore expected to have the wall located at larger radius than objects with low \dot{M} , increasing the total emitting area of the wall and thus the near-IR excess (Muzerolle et al. 2003; D'Alessio et al. 2004). This prediction has been confirmed by the Keck interferometer measurement of an inner structure at the expected location of the dust destruction radius in a high-accretion CTTS (Colavita et al. 2003; D'Alessio et al. 2004).

According to this model, the near-IR excess depends on the strength of the wall emission relative to photospheric fluxes. This emission is approximately that of a blackbody at the dust destruction temperature, $T_d \sim 1400$ K (Muzerolle et al. 2003), times the solid angle subtended by the wall. This solid angle is

essentially that of a cylinder of given height and radius equal to the dust destruction radius, with an inclination dependence that makes the emission reach a maximum at intermediate lines of sight ($60^{\circ}\text{--}80^{\circ}$) where the wall has maximum exposure (Dullemond et al. 2001; D'Alessio et al. 2004). The dust destruction radius is essentially $R_d \propto (L_* + L_{\text{acc}})^{1/2} / T_d^2$ (D'Alessio et al. 2004). The height of the wall z_w is estimated as the height where the radial optical depth from the star becomes ~ 1 (see Muzerolle et al. 2005).

We can examine the decrease of near-IR excesses with age in terms of these ideas. As they age, pre-main-sequence low-mass stars move down along Hayashi tracks essentially at constant T_{eff} while decreasing in luminosity. As \dot{M} decreases, L_{acc} becomes much smaller than L_* , so the dust destruction radius becomes fixed relative to the stellar radius, $R_d/R_* \propto L_*^{1/2} / T_d^2 R_* \sim (T_*/T_d)^2 \sim \text{constant}$. If the height of the wall is a fixed multiple of the disk scale height at R_d , which in turn is typically $\sim 0.1 R_d$, then the emitting area of the wall, $\propto R_d z_w$, and thus its total energy output, would decrease in the same proportion as the stellar output, namely $\propto R_*^2$. In this case, no decrease of near-IR excess relative to the photosphere with time would be expected. Since $R_d/R_* \sim \text{constant}$, the most natural way to explain the observed decrease is that the height of the wall z_w decreases with time. For this to happen, the opacity at the upper levels of the wall has to decrease, which implies that dust grains at the top of the wall significantly grow and/or settle toward the midplane as age increases.

Grain growth and/or settling toward the midplane in the disk regions outside the wall also results in low mid-IR fluxes. The disk is heated by stellar and accretion energy captured at the disk surface. Thus, heating of the disk depends on the shape of this surface; the more “flared” the surface is, the more energy it can capture (Kenyon & Hartmann 1987); disks with highly flared surfaces are hotter and thus emit more. To be more specific, the height of the surface z_s at a given radius is given by the condition that the radial optical depth to stellar radiation be ~ 1 . Since the density decreases with vertical height above the midplane, z_s decreases as the opacity of the dust in the upper layers decreases. Small grains have high opacity at wavelengths characteristic of the stellar radiation, in the optical and near-IR. They produce a highly flared surface, which results in more energy capture and hot and bright disks. In contrast, large grains have low opacity at short wavelengths. They produce flatter surfaces, which result in less energy capture and cooler and fainter disks (D01).

Alternatively, the opacity at upper layers may be reduced because grains are settling to the midplane. This also results in flatter surfaces and fainter disks in the IR (Dullemond & Dominik 2004). Both growth and settling are expected to occur together. Dust particles, affected by gas drag, collide and stick together; as the particles grow, they settle toward the midplane, falling under the effect of gravity (Weidenschilling & Cuzzi 1993; Weidenschilling 1997). These theories have many unknown parameters and so far predict timescales for complete settling of ≤ 1 Myr; however, the timescales depend on the magnitude of turbulence in disks, which could retard or prevent settling.

A number of claims of grain growth in disks have been made over the years, starting with the interpretation of slopes of the fluxes in the millimeter, which are expected to become flatter as the grain size increases (Beckwith & Sargent 1991). Assuming a dust mixture and a dust size distribution of the form $n(a) \propto a^{-p}$ between minimum and maximum sizes a_{min} and a_{max} , D01 find that a much better fit to the median SED of Taurus can

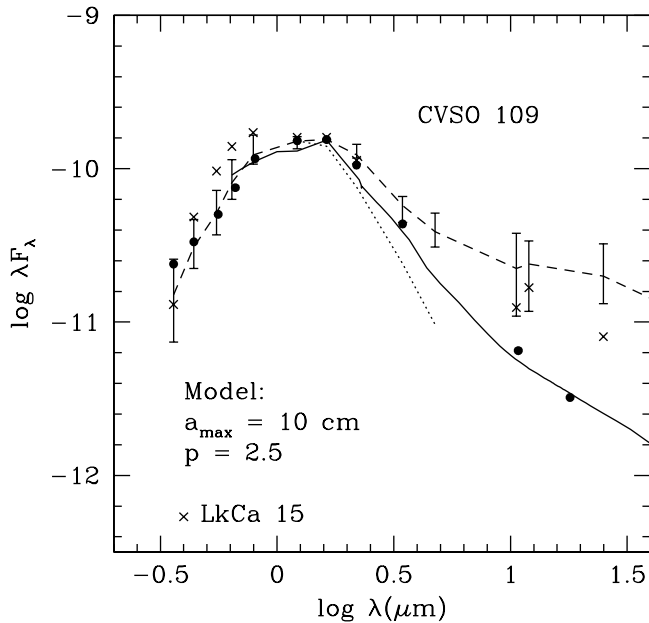


FIG. 10.—SED of CVSO 109 (*filled circles*) compared with the median of Taurus (*dashed line*), the photospheric fluxes (*dotted line*), and the SED of LkCa 15 (*crosses*). The solid line shows the SED of an irradiated accretion disk model with similar stellar and accretion parameters to CVSO 109 and with a dust size distribution characterized by $a_{\text{max}} = 10 \text{ cm}$ and exponent $p = 2.5$ (see text).

be achieved with dust particle growth to a maximum size a_{max} of 1 mm ($p = 3.5$) than with interstellar grains, with $a_{\text{max}} = 0.25 \mu\text{m}$. Grain growth and settling has been claimed to explain the SEDs of some CTTSs in Taurus. One well-studied case is that of the CTTS LkCa 15, which has a SED much flatter than the Taurus median in the IR and strong emission at submillimeter and millimeter wavelengths (Qi et al. 2003); the interpretation of this SED requires significant grain growth and settling (Chiang et al. 2001; D’Alessio et al. 2004; Bergin et al. 2004). In Figures 2–6 we have marked the location of LkCa 15; disks in Ori OB1 have similar colors to those of LkCa 15 in all bands, suggesting that significant dust evolution has also taken place in these older disks. In Figure 10 we compare the SED of CVSO 109, the only object for which we have detections up to $18 \mu\text{m}$, with fluxes for LkCa 15 from KH95 and with the Taurus median, both scaled to the H of CVSO 109. Note that LkCa 15 is a K5 star (KH95), so it is brighter in the optical than CVSO 109, which is an M0 star (Table 3). The SEDs of LkCa 15 and CVSO 109 are significantly lower than the Taurus median, although the flux deficit is much larger in CVSO 109.

To try to quantify the degree of dust evolution in CVSO 109, we have calculated models with uniformly distributed gas and dust following the procedures of D01. We have used stellar and accretion parameters from Table 3 and have varied the parameters a_{max} and p , which characterize the dust size distribution. Figure 10 shows our best model. To fit the observed fluxes, we require $a_{\text{max}} = 10 \text{ cm}$; this is higher than the maximum sizes required to explain the median SED in Taurus, $a_{\text{max}} \sim 1 \text{ mm}$ (D01), or the SED of the $\sim 10 \text{ Myr}$ old star TW Hya, $a_{\text{max}} \sim 1 \text{ cm}$ (Calvet et al. 2002; Wilner et al. 2000). Moreover, we require $p = 2.5$, a value consistent with significant dust coagulation (Miyake & Nakagawa 1995); modeling of CTTS disks can generally be carried out successfully with the assumption of $p = 3.5$, a value characteristic of the interstellar medium (cf. D01; Chiang et al. 2001).

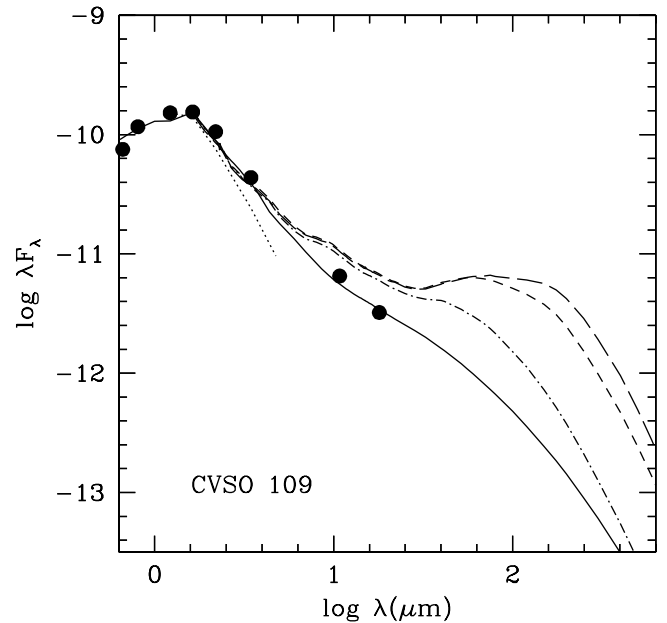


FIG. 11.—Effect of disk radius on SED: disk models for $a_{\text{max}} = 1 \text{ mm}$, $p = 3.5$, and disk radius 100 AU (*long-dashed line*), 50 AU (*short-dashed line*), and 10 AU (*dot-dashed line*); model for $a_{\text{max}} = 10 \text{ cm}$ and $p = 2.5$ (*solid line*); and observations of CVSO 109 (*circles*). The photosphere is indicated by the dotted line.

Our modeling is only indicative in that we have assumed that the dust is uniformly distributed with the gas. Even with this assumption, our comparison implies that the disk of CVSO 109 is essentially a flat disk, with little if any flaring. Thus, our modeling indicates that the dust in the disk of CVSO 109 has strongly settled toward the midplane, as expected from theories of dust evolution in protoplanetary disks (Weidenschilling 1997). Models including settling in addition to observations at longer wavelengths are required to actually constrain the size distribution of the solids in the midplane.

A possible alternative to consider is that disks in Ori OB1 are smaller than their Taurus counterparts because their outer parts have been photoevaporated by the external ionizing fields of the high-mass stars in the associations. A smaller disk would have less emission at long wavelengths, since the low-temperature regions would be removed. Models for the viscous evolution of disks subject to the effects of photoevaporating radiation fields from the accretion flows and external radiation fields have been calculated by Clarke et al. (2001) and Matsuyama et al. (2003). Since the distance from the ionizing stars are of the order of a few pc in OB associations, far-ultraviolet (FUV) external photons are expected to dominate over extreme ultraviolet photons in the photoevaporation of disks (Johnstone et al. 1998). For this case, Matsuyama et al. (2003) find that the outer portions of the disk could be removed on timescales that range from 1 to several megayears, depending on the viscosity parameter. After significant photoevaporation, the disk edge is fixed by the FUV gravitational radius, which for parameters like those of the Ori OB1b stellar sample is $\sim 30 \text{ AU}$. To determine the effects of a reduction of disk radius on the SED, and in particular to see if a smaller disk radius can explain the low mid-IR fluxes without extreme grain growth, we have calculated disk models with $a_{\text{max}} = 1 \text{ mm}$ and $p = 3.5$, characteristic of the Taurus population, for disk radii of 100, 50, and 10 AU. These SEDs are shown in Figure 11. Models are calculated at a high inclination to the line of sight (72°) to maximize the contrast between the star and the disk. Even

small disks produce too much long-wavelength flux compared with the observations, if $a_{\max} = 1$ mm as in Taurus. This implies again that the disk has to be essentially flat, which requires that grains grow to larger sizes and/or have settled.

5. SUMMARY AND CONCLUSIONS

We have detected clear signatures of disk evolution in samples of accreting stars in the Ori OB1a and 1b associations, with ages 7–10 and 3–5 Myr, respectively. The mass accretion rates of these stars are consistent with viscous evolution of accretion disks. In addition, we find a significant overall decrease of IR emission with age. Comparison with disk models indicates that grain growth and settling, processes expected from dust evolution, are responsible for this decrease. Future observations of larger samples of Ori OB1 stars with *Spitzer* will provide more detail on the nature of the dust evolution process.

We thank the referee for many useful suggestions. This work was supported by NSF grant AST 99-87367 and NASA grant

NAG5-10545. P. D. acknowledges grants from PAPIIT, DGAPA (UNAM), and CONACyT, Mexico. This paper is based on observations obtained at the Gemini Observatory, which is operated by the Association of Universities for Research in Astronomy, Inc., under a cooperative agreement with the National Science Foundation (NSF) on behalf of the Gemini partnership: the NSF (United States), the Particle Physics and Astronomy Research Council (United Kingdom), the National Research Council (Canada), CONICYT (Chile), the Australian Research Council (Australia), CNPq (Brazil) and CONICET (Argentina). This research makes use of data products from 2MASS, which is a joint project of the University of Massachusetts and the Infrared Processing and Analysis Center/California Institute of Technology, funded by NASA and the National Science Foundation. This paper is based on observations obtained with the mid-IR camera OSCIR, developed by the University of Florida with support from NASA and operated jointly by Gemini and the University of Florida Infrared Astrophysics Group. This research has made use of the SIMBAD database, operated at CDS, Strasbourg, France.

REFERENCES

- Alibert, Y., Mordasini, C., & Benz, W. 2004, *A&A*, 417, L25
- Bally, J., Stark, A. A., Wilson, R. W., & Langer, W. D. 1987, *ApJ*, 312, L45
- Barden, S., & Armandroff, T. 1995, *Hydra/WIYN Users Manual* (Tucson: NOAO)
- Beckwith, S. V. W., & Sargent, A. I. 1991, *ApJ*, 381, 250
- Bergin, E., et al. 2004, *ApJ*, 614, L133
- Blaauw, A. 1964, *ARA&A*, 2, 213
- Briceño, C., Calvet, N., Hernández, J., Vivas, A. K., Hartmann, L., Downes, J. J., & Berlind, P. 2005, *AJ*, 129, 907 (Paper I)
- Briceño, C., et al. 2001, *Science*, 291, 93
- Brown, A. G. A., de Geus, E. J., & de Zeeuw, P. T. 1994, *A&A*, 289, 101
- Calvet, N., D'Alessio, P., Hartmann, L., Wilner, D., Walsh, A., & Sitko, M. 2002, *ApJ*, 568, 1008
- Calvet, N., & Gullbring, E. 1998, *ApJ*, 509, 802
- Cardelli, J. A., Clayton, G. C., & Mathis, J. S. 1989, *ApJ*, 345, 245
- Carpenter, J. M. 2001, *AJ*, 121, 2851
- Chiang, E. I., Joungh, M. K., Creech-Eakman, M. J., Qi, C., Kessler, J. E., Blake, G. A., & van Dishoeck, E. F. 2001, *ApJ*, 547, 1077
- Clarke, C. J., Gendrin, A., & Sotomayor, M. 2001, *MNRAS*, 328, 485
- Cohen, M., Walker, R. G., Carter, B., Hammersley, P., Kidger, M., & Noguchi, K. 1999, *AJ*, 117, 1864
- Colavita, M., et al. 2003, *ApJ*, 592, L83
- D'Alessio, P., Calvet, N., & Hartmann, L. 2001, *ApJ*, 553, 321 (D01)
- D'Alessio, P., Calvet, N., Hartmann, L., Lizano, S., & Cantó, J. 1999, *ApJ*, 527, 893
- D'Alessio, P., Calvet, N., Hartmann, L., Muzerolle, J., & Sitko, M. 2004, in *IAU Symp. 221, Star Formation at High Angular Resolution*, ed. M. Burton, R. Jayawardhana, & T. Bourke (San Francisco: ASP), 403
- D'Alessio, P., Cantó, J., Calvet, N., & Lizano, S. 1998, *ApJ*, 500, 411
- D'Antona, F., & Mazzitelli, I. 1994, *ApJS*, 90, 467
- de Zeeuw, P. T., Hoogerwerf, R., de Bruijne, J. H. J., Brown, A. G. A., & Blaauw, A. 1999, *AJ*, 117, 354
- Dolan, C. J., & Mathieu, R. D. 1999, *AJ*, 118, 2409
- . 2001, *AJ*, 121, 2124
- . 2002, *AJ*, 123, 387
- Dullemond, C. P., & Dominik, C. 2004, *A&A*, 421, 1075
- Dullemond, C. P., Dominik, C., & Natta, A. 2001, *ApJ*, 560, 957
- Elias, J. H., Frogel, J. A., Matthews, K., & Neugebauer, G. 1982, *AJ*, 87, 1893
- Fabricant, D., Cheimets, P., Caldwell, N., & Geary, J. 1998, *PASP*, 110, 79
- Gullbring, E., Calvet, N., Muzerolle, J., & Hartmann, L. 2000, *ApJ*, 544, 927
- Gullbring, E., Hartmann, L., Briceño, C., & Calvet, N. 1998, *ApJ*, 492, 323
- Haisch, K. E., Lada, E. A., & Lada, C. J. 2001, *ApJ*, 553, L153
- Hartigan, P., Edwards, S., & Ghandour, L. 1995, *ApJ*, 452, 736
- Hartigan, P., Kenyon, S. J., Hartmann, L., Strom, S. E., Edwards, S., Welty, A. D., & Stauffer, J. 1991, *ApJ*, 382, 617
- Hartmann, L. 1998, *Accretion Processes in Star Formation* (Cambridge: Cambridge Univ. Press)
- Hartmann, L. 2003, *ApJ*, 585, 398
- Hartmann, L., Calvet, N., Gullbring, E., & D'Alessio, P. 1998, *ApJ*, 495, 385
- Hillenbrand, L. A. 1997, *AJ*, 113, 1733
- Hillenbrand, L. A., Strom, S. E., Vrba, F. J., & Keene, J. 1992, *ApJ*, 397, 613
- Hillenbrand, L. A., et al. 2005, in preparation
- Johnstone, D., Hollenbach, D., & Bally, J. 1998, *ApJ*, 499, 758
- Kenyon, S. J., & Hartmann, L. 1987, *ApJ*, 323, 714
- . 1995, *ApJS*, 101, 117 (KH95)
- Landolt, A. U. 1992, *AJ*, 104, 340
- Matsuyama, I., Johnstone, D., & Hartmann, L. 2003, *ApJ*, 582, 893
- Meyer, M., Calvet, N., & Hillenbrand, L. A. 1997, *AJ*, 114, 288
- Millan-Gabet, R., Schloerb, F. P., Traub, W. A., Malbet, F., Berger, J. P., & Bregman, J. D. 1999, *ApJ*, 513, L131
- Miyake, K., & Nakagawa, Y. 1995, *ApJ*, 441, 361
- Monnier, J. D., & Millan-Gabet, R. 2002, *ApJ*, 579, 694
- Muzerolle, J., Calvet, N., Briceño, C., Hartmann, L., & Hillenbrand, L. 2000, *ApJ*, 535, L47
- Muzerolle, J., D'Alessio, P., Calvet, N., & Hartmann, L. 2005, *ApJ*, in press
- Meyer, M., Calvet, N., Hartmann, L., & D'Alessio, P. 2003, *ApJ*, 597, L149
- Muzerolle, J., Hillenbrand, L., Calvet, N., Hartmann, L., & Briceño, C. 2001, in *ASP Conf. Ser. 244, Young Stars Near Earth: Progress and Prospects*, ed. R. Jayawardhana & T. Greene (San Francisco: ASP), 245
- Natta, A., Prusti, T., Neri, R., Wooden, D., Grinin, V. P., & Mannings, V. 2001, *A&A*, 371, 186
- Podosek, F. A., & Cassen, P. 1994, *Meteoritics*, 29, 6
- Pollack, J., Hubickyj, O., Bodenheimer, P., Lissauer, J., Podolak, M., & Greenzweig, Y. 1996, *Icarus*, 124, 62
- Qi, C., Kessler, J. E., Koerner, D. W., Sargent, A. I., & Blake, G. A. 2003, *ApJ*, 597, 986
- Rice, W. K. M., Wood, K., Armitage, P. J., Whitney, B. A., & Bjorkman, J. E. 2003, *MNRAS*, 342, 79
- Schlegel, D. J., Finkbeiner, D. P., & Davis, M. 1998, *ApJ*, 500, 525
- Sicilia-Aguilar, A., et al. 2005, in preparation
- Siess, L., Dufour, E., & Forestini, M. 2000, *A&A*, 358, 593
- Tollestrup, E. V., & Willner, S. P. 1998, *Proc. SPIE*, 3354, 502
- Tuthill, P. G., Monnier, J. D., & Danchi, W. C. 2001, *Nature*, 409, 1012
- Warren, W. H., & Hesser, J. E. 1977, *ApJS*, 34, 115
- . 1978, *ApJS*, 36, 497
- Weidenschilling, S. J. 1997, *Icarus*, 127, 290
- Weidenschilling, S. J., & Cuzzi, J. N. 1993, in *Protostars and Planets III*, ed. E. H. Levy & J. I. Lunine (Tucson: Univ. Arizona Press), 1031
- Wilner, D. J., Ho, P. T. P., Kastner, J. H., & Rodríguez, L. F. 2000, *ApJ*, 534, L101
- Wood, J. 2004, in *AIP Conf. Proc. 713, The Search for Other Worlds*, ed. S. S. Holt & D. Deming (New York: AIP), 73